Atmos. Chem. Phys. Discuss., 14, 1239–1285, 2014
www.atmos-chem-phys-discuss.net/14/1239/2014/
doi:10.5194/acpd-14-1239-2014
© Author(s) 2014. CC Attribution 3.0 License.

Atmospheric Chemistry and Physics Discussions
Open Access

This discussion paper is/has been under review for the journal Atmospheric Chemistry and Physics (ACP). Please refer to the corresponding final paper in ACP if available.

On the temporal variability of the OH* emission layer at the mesopause: a study based on SD-WACCM4 and SABER

S. Kowalewski[1], C. von Savigny[2], M. Palm[1], and J. Notholt[1]

[1]Institute of Environmental Physics, University of Bremen, Bremen, Germany
[2]Institute of Physics, Ernst-Moritz-Arndt-University of Greifswald, Greifswald, Germany

Received: 15 November 2013 – Accepted: 4 January 2014 – Published: 16 January 2014

Correspondence to: S. Kowalewski (kowalewski@iup.physik.uni-bremen.de)

Published by Copernicus Publications on behalf of the European Geosciences Union.

Abstract

Airglow observations are a fundamental tool to study the mesospheric part of the atmosphere. In particular the OH* emission layer is subject of many theoretical and observational studies. The choice of different transition bands of the OH* emission can introduce systematic differences between these studies, hence a profound knowledge of these differences is required for comparison. One systematic difference is given by the vertical displacements between OH* profiles due to different transition bands. A previous study has shown that the vertical displacement is highly sensitive to quenching with atomic oxygen. In this work we follow up this idea by investigating the diurnal as well as the seasonal response of OH* to changes in concentrations of atomic and molecular oxygen, the two most effective quenching species of OH*. For this task we employ a quenching model to calculate vertical OH* concentration profiles from simulations made with the SD-WACCM4 chemistry transport model. From this approach we find that despite the strong impact of O and O_2 quenching on the vertical OH* structure, a considerable variability between the vertical displacements of different OH* transition bands is also induced by the natural variability of the O_3 and H profiles, which primarily participate in the formation of the mesospheric OH* layer. This in particular applies for the diurnal evolution of the vertical displacements, which cannot be explained by changes in abundances of OH* quenching species only. On the other hand, vertical displacements between OH* transition bands and the amount of effective O and O_2 quenching show a coherent semi-annual oscillation at lower latitudes that is in phase with the seasonal variability of the diurnal migrating tide. In particular the role of O_2 quenching shows a new aspect of the semi-annual oscillation that, to our knowledge, has not been discussed before. By comparison with limb radiance observations from the SABER/TIMED satellite, we find evidence for the same oscillation in the vertical displacement between different OH* transition bands and derived O concentrations. However, our model study also reveals that quenching is not the only driving process of this feature.

ACPD
14, 1239–1285, 2014

1 Introduction

The hydroxyl emission layer is a prominent feature of the mesopause region. Its main production process is commonly referred to as the Bates–Nicolet mechanism (McDade, 1991). This mechanism suggests the exothermic reaction between O_3 and H, which leads to rotational-vibrationally excited OH* radicals (Bates and Nicolet, 1950). According to the available exothermic energy of this reaction, these radicals can have excited vibrational states up to the $v = 9$ quantum number. Lower vibrational states can be populated via spontaneous emission, but also through quenching with ambient species. Hence, we can distinguish between different OH(v) layers with respect to their vibrational excitation states.

Because different observational studies on the mesospheric OH* emission can rely on different transition bands, it is of general interest to understand differences between these OH(v) layers. Previous studies have shown that quenching with ambient species is significantly affecting the relative vertical positions between different OH(v) layers (e.g. Dodd et al., 1994; Makhlouf et al., 1995, and Adler-Golden, 1997). In particular atomic oxygen is an effective quencher and its impact on the vertical distribution of different OH(v) layers has been recently investigated by von Savigny et al. (2012). Based on a sensitivity study, which relies on an updated version of the McDade quenching model (McDade, 1991), they suggest that quenching with atomic oxygen causes an upward shift of the individual OH(v) layers with increasing vibrational state. In a follow-up study, von Savigny and Lednyts'kyy (2013) provided experimental evidence, that the vertical shifts between different OH* bands are indeed correlated with the amount of atomic oxygen in the altitude range, where the OH* emission occurs.

In this study we reexamine this idea by investigating the temporal evolution of the OH(v) layers and their responsiveness to changes in atomic oxygen concentrations. In addition, we will also investigate the importance of quenching with molecular oxygen, which is another effective quencher of OH* (Adler-Golden, 1997). For our investigation we use chemical profiles and temperature fields from simulations made with the

ACPD
14, 1239–1285, 2014

Whole Atmosphere Community Climate Model driven with Specified Dynamical fields (SD-WACCM4). We modify the McDade quenching model such that we can calculate (offline) OH(v = 1, 2, . . . , 9) absolute number concentrations from the SD-WACCM4 simulations, which we compare with limb radiance observations from the SABER (Sounding of the Atmosphere by Broadband Emission Radiometry) instrument onboard of the TIMED (Thermosphere Ionosphere Mesosphere Energetics Dynamics) satellite. Two SABER channels exist, which can sense OH* emissions from different transition bands simultaneously, hence, we can compare the vertical shifts between these emissions with our simulated OH(v) layers and investigate their response to temporal changes in atomic oxygen concentrations. Because of the still remaining difficulties in modeling but also measuring atomic oxygen, we include atomic oxygen profiles to our investigation from both, SD-WACCM4 simulations and SABER observations. Following the study on OH* airglow variability by Marsh et al. (2006), we put our focus on the diurnal as well as the seasonal variability of OH* with special emphasis on quenching with atomic and molecular oxygen.

This paper is structured as follows. Section 2 introduces our OH quenching model and gives a brief summary on the SD-WACCM4 and SABER data, which we include in our intercomparison study. In Sect. 3, we discuss the general features of the vertical OH* profiles based on a case example in our model study. This includes a first investigation of the diurnal evolution of the vertical shifts between two OH(v) layers of different vibrational excitation with respect to changes in O and O_2 concentrations. We expand our analysis to the available data range in Sect. 4 and compare seasonal signatures in vertical OH* (v) layer shifts between our model results and SABER observations. In the final Sect. 5, we give a summary of our main findings and discuss their implications for our understanding of the temporal variability of the OH* layer.

ACPD
14, 1239–1285, 2014

2 Model and data description

2.1 Hydroxyl quenching model

A detailed description of the McDade model, which we use as a basis for our OH* simulations, is given in McDade and Llewellyn (1988) and McDade (1991). Here, we limit our discussion to its primary key aspects and our adjustments to simulate absolute number concentrations of OH(v).

As mentioned in the beginning, the Bates–Nicolet mechanism suggests the principal excitation mechanism of vibrationally excited OH* according to the following reaction:

$$H + O_3 \rightarrow OH(v' \leq 9) + O_2 \qquad k_1 \quad \text{(R1)}$$

where k_1 denotes the rate constant of this reaction. The released exothermic energy of this reaction leads to a preferred vibrational excitation between $v = 6$ and $v = 9$. In accordance with von Savigny et al. (2012) we assume the following processes to populate lower vibrational states:

- radiative cascade from the initially populated higher levels

$$OH(v') \rightarrow OH(v'') + h\nu \qquad A(v', v'') \quad \text{(R2)}$$

- collisional relaxation

$$OH(v') + Q \rightarrow OH(v'') + Q \qquad k_3^Q(v', v'') \quad \text{(R3)}$$

with $Q = O_2, N_2$.

- complete OH removal

$$OH(v') + Q \rightarrow \text{other products} \qquad k_4^Q(v', v'') \quad \text{(R4)}$$

with $Q = O, O_2, N_2$.

ACPD
14, 1239–1285, 2014

Apart from these processes, the recombination of the perhydroxyl radical (HO_2) with atomic oxygen as being proposed by Krassovsky (1963) could provide another mechanism to form OH* with vibrational excitations below $v = 6$ at the mesopause. Different opinions exist on the importance of this mechanism to the general OH* formation (e.g. see Khomich et al., 2008, for a summary of different studies), though the recent study by Xu et al. (2012) implicates that its contribution is rather negligible for vibrational states above $v = 3$. As we will discuss later, the main emphasis of our study is on vibrational states above $v = 3$, accordingly we neglect this mechanism in our following considerations.

Following McDade (1991), Eq. (3) in von Savigny et al. (2012) describes the OH* concentration for steady state conditions. Here, we adjust this expression as follows:

$$[\mathrm{OH}(v)] = \left(A(v) + \sum_{\mathrm{Q}} k_L^{\mathrm{Q}}(v)[\mathrm{Q}]\right)^{-1} \times \left(P(v)\{k_1[\mathrm{H}][\mathrm{O}_3]\} + \sum_{v^*=v+1}^{9} [\mathrm{OH}(v^*)]\{A(v^*,v) + \sum_{\mathrm{Q}} k_3^{\mathrm{Q}}(v^*,v)[\mathrm{Q}]\}\right) \quad (1)$$

where P is the nascent vibrational level distribution, $A(v)$ corresponds to the inverse radiative lifetime of OH and k_L^{Q} is the total rate constant for removal of OH in vibrational level v through Reactions (R3) and (R4). Accordingly, we substitute the nascent production rate p in von Savigny et al. (2012) by the $P(v)\{k_1[\mathrm{H}][\mathrm{O}_3]\}$ rate term in the nominator of Eq. (1). In contrast to the work of von Savigny et al. (2012), we do not normalise Eq. (1) with respect to the $v = 9$ vibrational state, therefore we have to implement absolute rate constants as well as absolute inverse radiative lifetimes in our equation.

For our present model simulations we use the constants listed in Table 1, assuming that multiquantum relaxation only applies for quenching with O_2, while the less efficient N_2 quenching is limited to single-quantum relaxation only. If we apply these assumptions to Eq. (1), we get the following expression for OH* as a function of vibrational

ACPD
14, 1239–1285, 2014

state:

$$[\mathrm{OH}(v)] = \left(A(v) + k_L^{\mathrm{O}_2}(v)[\mathrm{O}_2] + k_L^{\mathrm{N}_2}(v)[\mathrm{N}_2] + k_L^{\mathrm{O}}(v)[\mathrm{O}]\right)^{-1} \times$$
$$\left(P(v)\{k_1[\mathrm{H}][\mathrm{O}_3]\} + \sum_{v^*=v+1}^{9} [\mathrm{OH}(v^*)]\{A(v^*,v) + k_3^{\mathrm{O}_2}(v^*,v)[\mathrm{O}_2] + k_3^{\mathrm{N}_2}(v^*,v)[\mathrm{N}_2]\}\right) \quad (2)$$

with $k_3^{\mathrm{N}_2}(v^*,v) = 0$ for all $\{v^* > v+1\}$ and $k_3^{\mathrm{N}_2}(v^*,v) = k_L^{\mathrm{N}_2}(v^*)$ for $\{v^* = v+1\}$.

2.2 SD-WACCM4

The SD-WACCM4 simulations are based on the Whole Atmosphere Community Model, version 4 (WACCM4), which is a comprehensive free-running chemistry-climate model. This model version is based on an earlier version described by Garcia et al. (2007) and has been recently extended, such that it is nudged to meteorological fields that are taken from the Global Earth Observing System Model, Version 5 (GEOS-5) of NASA's Global Modeling and Assimilation Office (GMAO).

SD-WACCM4 data were provided to us by courtesy of R. R. Garcia and D. E. Kinnison, NCAR Boulder. The same SD-WACCM4 simulations, which we consider in our study, were already applied to another study by Hoffmann et al. (2012) that investigates the dynamics of the model using mesospheric CO VMR measurements. We therefore refer to this paper for a more detailed description of the model. Here, we limit our discussion to the most relevant aspects to our study.

According to the "specified dynamics", which are introduced by the SD-WACCM4 version, the WACCM4 model essentially turns into a chemical transport model. The nudging of GEOS-5 data within SD-WACCM4 is constrained from the surface to 50 km altitude, with a linearly decreasing relaxation scheme until it completely switches to a free-running mode above 60 km. According to the study of Hoffmann et al. (2012) they show that the upper (free-running) part is strongly driven by the described nudging.

ACPD
14, 1239–1285, 2014

The horizontal resolution of the SD-WACCM4 data is 1.9° × 2.5° in latitude and longitude. Its vertical extent reaches from the ground up to the lower thermosphere at about 140 km geometrical height and it is divided into 66 height levels. In the region from 80 km up to 95 km, which encloses the hydroxyl emission, the vertical distance between the model grid points varies from about 1.2 km to 3.6 km. The SD-WACCM4 simulations are initially performed at 0.5 h time increments, however, to save computational resources, global model results are stored as daily increments at 00:00 UTC. This limitation of our dataset prevents us from studying the diurnal evolution of the OH* vertical profiles at a fixed geolocation. To overcome this constraint we may assume that the diurnal evolution of the vertical profiles is already contained within the zonal variation of each daily model result, i.e. we convert the longitudinal information to the Local Solar Time (LST). However, as we will discuss in Sect. 3.4, other processes exist, which can still complicate a comparison of the diurnal variability between SD-WACCM4 and SABER.

To simulate OH(v) profiles by means of Eq. (2), we use the O_3, H and O profiles from the SD-WACCM4 simulations. In addition we use SD-WACCM4 pressure and temperature fields to convert these profiles to absolute number densities. Accordingly, we derive number density profiles of the remaining O_2 and N_2 quenching species from their constant VMRs. The SD-WACCM4 data in this study cover the period between April 2010 and June 2011.

2.3 SABER

SABER is a multichannel infrared radiometer onboard of the TIMED satellite. Limb profiles are taken from a circular orbit at 625 km inclined at 74° to the equator and cover a latitudinal range from 54° S to 82° N or 82° S to 54° N, depending on the phase of the yaw cycle (Russell III et al., 1999). One yaw cycle of SABER corresponds to 60 days, i.e. due to the full precession of the instrument during one cycle, this period is required to get a full coverage of local times.

ACPD
14, 1239–1285, 2014

SABER is equipped with two channels sensitive to OH* emissions, i.e. the 1.6 µm channel covers emissions from the OH(5-3)/OH(4-2) transitions and the 2.0 µm channel covers emissions from the OH(9-7)/OH(8-6) transitions.

Volume-Emission-Rate (VER) profiles from both channels are contained in the SABER Level 2a data products and will be used in our study. According to Mertens et al. (2009) the vertical resolution of the SABER VER profiles is approximately 2 km. Because the atmosphere is optically thin at altitudes above 80 km for wavelengths between 0.35 and 2.0 µm (Khomich et al., 2008), the effect of self-absorption is negligible for the observed OH* emission. Given this assumption, we can directly compare changes in our simulated OH* concentrations to changes in the vertical VER profiles.

In addition to measurements of the OH* radiance, the latest SABER V2.0 data contain atomic oxygen profiles, which we include to our study as mentioned before. Because of the difficulties in directly measuring the atomic oxygen species, these profiles are derived from the OH* radiance during nighttime as described in Mlynczak et al. (2013).

3 Diurnal variability: a monthly case example

3.1 Vertical OH* structure

For the first part of this study we will discuss some general features of simulated vertical OH* profiles. Figure 1 shows two examples of vertical vibrational populations with one referring to nighttime conditions (upper panels) and the other referring to daytime conditions (lower panels). In accordance with von Savigny et al. (2012) the nighttime vibrational populations form single peak profiles that are shifted upwards with respect to their vibrational state (upper right panel). Moreover, the vertical shift between different vibrational populations is more pronounced above their peak altitudes. Based on a sensitivity study, von Savigny et al. (2012) relate this asymmetry in the vertical shifts mainly to the steep vertical gradient in O concentrations and the associated k_L^O rate

ACPD
14, 1239–1285, 2014

constant. With respect to our daytime example, we can find a secondary peak that is particularly pronounced for lower vibrational states. If we limit our comparison to the main peak of day- and nighttime profiles, we can see that absolute nighttime concentrations generally exceed daytime concentrations. This is something we would expect, because the loss of O_3 due to photodissociation during sunlit conditions is directly impacting Reaction (R1). Interestingly, absolute daytime concentrations appear to exceed nighttime concentrations, where they form the secondary peak at about 62 km. A similar daytime profile structure is shown in a model study of Funke et al. (2012), which is also accounting for non-LTE conditions in its algorithms. They argue that the lower daytime peak results from the larger daytime H abundances, which we can also find in the SD-WACCM 4 profiles.

In the following, we will mainly focus on nighttime OH*, because the relatively low abundances of daytime OH* and the large Rayleigh scattering background make OH* daytime observations very difficult.

3.2 OH* concentrations and emission peak altitudes

Before we will address the temporal evolution of individual OH(v) vertical profiles, we first consider the sum over all vibrational OH($v = 1, 2, \ldots, 9$) profiles. Figure 2 shows an example of simulated OH*, where the upper left panel refers to a monthly mean and the upper right panel refers to an arbitrary daily sample within the same monthly mean to illustrate some of its fine scale features.

One can clearly see the sharp day/night transition from low to high OH* concentrations in both panels. Interestingly, for the daily sample we can find at mid-southern latitudes some striking synoptic scale daytime features of exceptionally high OH* concentrations similar to nighttime concentrations. These features still remain, if we consider individual vibrational levels (not shown) and can persist for a few days. Similar features, but less pronounced, can be seen during the boreal summer at northern mid-latitudes. However, we cannot exclude that these localised high daytime concentrations might represent a model feature due to the free-running mode of SD-WACCM4 above

ACPD
14, 1239–1285, 2014

60 km. Because of our emphasis on nighttime concentrations, we keep these features as a note.

For nighttime OH*, we can see a general eastward decrease in the vertically integrated concentrations. We can find a similar trend for all months throughout the year, but the high OH* concentrations ranging from central Asia to Siberia appear to be a special feature of this month.

According to our previous discussion, we can interpret the eastward decrease in OH* concentrations as a nighttime decrease by converting the longitudes in Fig. 2 to local times. In addition to the decreasing nighttime trend, we can also find enhanced OH* concentrations at the equatorial regions, which minimise at around ±30°. This latitudinal structure is consistent with the study of Marsh et al. (2006) and other observational studies stated therein.

Previous studies based on observations made with the high-resolution Doppler imager (HRDI) instrument and the Wind Imaging Interferometer (WINDII) instrument onboard the upper atmosphere research satellite (UARS) revealed that the peak altitude of the OH* emission layer increases with decreasing integrated emission rate, which is explained by the vertical motions associated with tides or other processes (see Cho and Shepherd, 2006; Liu and Shepherd, 2006 and references therein). To check as to whether our simulated vertical OH* profiles are consistent with this finding, we determine the peak altitude of each profile by weighting the geometric heights with the vertical OH* number density profiles. Based on this method, the lower left panel of Fig. 2 shows the monthly average of our weighted peak altitudes. If we exclude the region of enhanced OH* concentrations above central Asia and Siberia, we can see that peak altitudes increase over the course of the night by up to 4 km. In contrast, the area of enhanced OH* concentrations above central Asia and Siberia shows a pronounced drop in peak altitudes. This clearly reflects the inverse relationship between peak altitudes and integrated OH* concentrations, which is consistent with the findings mentioned in Liu and Shepherd (2006). Before discussing the relative vertical displacement between different OH(v) layers in the next section, we have to address another

ACPD
14, 1239–1285, 2014

important aspect with regard to the OH* profile shape. If we remember the double peak structure of the daytime OH* profile according to Fig. 1, in this case the determination of peak altitudes by weighting the whole vertical profile would appear less meaningful. In general, the existence of multiple peak structures in the vertical OH* profiles would complicate the comparison between different OH(v)* layers, thus, affecting our study on the OH* quenching process in the following sections. However, according to our nighttime example in Fig. 1 we may assume that nighttime OH* profiles generally follow a single peak shape. To validate this assumption, we have counted the number of local maxima of each vertical OH* number density profile that occurs above 50 km altitude. Furthermore, local maxima must have amplitudes of at least 10 % with respect to the largest peak of the vertical OH* number density profile. Based on these counting rules, the lower right panel in Fig. 2 shows the monthly average of daily peak counts. As we can see, indeed the nighttime vertical OH* profiles mainly consist of single peaks, hence, we should expect no significant interference with our peak altitude determination method during the nighttime. Only around the early evening hours at mid and high northern latitudes, occasionally multiple peak structures appear in the vertical OH* profiles but the overall contribution remains low. Furthermore, we find the same dominating single peak structure for the other months of our dataset (not shown). In addition to the validation of our assumption on the single peak shape of nighttime OH* profiles, this finding could also have an interesting implication for observational studies that report noticeable amounts of complex multiple peak structures in the vertical OH* VER profiles during nighttime (e.g. Melo et al., 2000 report such structures for up to 25 % of their examined WINDII profiles). Because these complex structures can either result from vertical or lateral inhomogeneities, the dominant single peak shape we find in the vertical OH* WACCM profiles would suggest the latter case.

3.3 Vertical displacements of OH(v)

As motivated in the beginning, the relative vertical displacements between the OH(v) layers can be significantly affected by quenching with atomic oxygen, in particular

ACPD
14, 1239–1285, 2014

above the peak altitudes. We further refine our study by focusing on two different vibrational states in the following.

To allow a later comparison with SABER VER measurements, we select the OH(9) and OH(5) layers, because they both contain emissions, which can be observed by the 1.6 and 2.0 µm SABER channels separately. Ideally, one must consider that each SABER channel captures a mixture of emissions that belong to two different transition bands. However, because the difference in vibrational levels between each transmission is limited to $\Delta\nu = 1$, we assume that we can neglect the effect of profile mixing for each channel, if we are interested in the relative vertical displacement between both (mixed) OH* profiles.

In order to determine the vertical displacement between two OH* layers, we can subtract their corresponding (profile) weighted geometric altitudes from each other. On the other hand, our case example of a vertical OH* profile according to Fig. 1 illustrates that the vertical spread between different OH(ν) layers increases with height due to the increase in the effective O quenching that results from the steep vertical gradient of O concentrations. For our study on the response of the relative distance between the OH(9) and OH(5) layers to changes in O concentrations, this seems to favor a comparison between the upper parts of both layers. To account for this, we can interpolate the altitudes, where both OH(ν) number density/VER profiles have dropped by a factor of 0.5 relative to the OH* number density/VER profile peak value, which we will refer to as the Half Width at Half Maximum (HWHM) in the following. However, as we will soon discuss, this criterion to determine the vertical displacement between both layers is also highly sensitive to relative changes in the profile shapes, which could affect the correlation with changes in atomic oxygen. On the other hand, changes in the relative layer widths should have a less pronounced effect for the weighted peak altitudes, but the vertical spread between different OH(ν) layers is less pronounced. It is for this reason that we decided to include both definitions in our study to investigate, which of them appears to be more suitable to compare changes in peak shifts with changes in O concentrations.

ACPD
14, 1239–1285, 2014

Fig. 3 shows determined values of vertical shifts $\Delta Z_{9,5}$ between simulated OH* profiles for the same temporal average as being considered in Fig. 2. For the vertical shift between weighted peak altitudes, we can find a general decrease in $\Delta Z_{9,5}$ values over the course of the night. In contrast, the nighttime evolution of $\Delta Z_{9,5}$ at the upper part of the OH* layer is more complex. To relate the nighttime evolution of vertical shifts with changes in O, we choose to calculate O concentrations by weighting their vertical profiles with the OH(9) concentrations in Fig. 3. We will also address other methods to account for temporal changes in O concentrations at the end of this section.

By comparison with the lower panel in Fig. 3, we can see that the diurnal evolution of weighted O can hardly explain the rather monotonic decrease in nighttime $\Delta Z_{9,5}$ for weighted peak altitudes. The situation still remains difficult when considering $\Delta Z_{9,5}$ for HWHM shifted peak altitudes. If we focus again on north-eastern latitudes, we can see a striking maximum of weighted O concentrations. The decrease in OH* layer altitudes in the same region could reflect an enhanced downward transport that is driven by strong advection from lower latitudes according to Smith et al. (2011). In comparison, the response in $\Delta Z_{9,5}$ for HWHM shifted peak altitudes is not as pronounced for this region, though values are relatively high. In addition, the variability in $\Delta Z_{9,5}$ is larger than for weighted O concentrations, hence, the diurnal response to O quenching appears to be less evident than initially expected.

To gain a better understanding of the actual impact of O quenching on the diurnal evolution of $\Delta Z_{9,5}$, we investigate its sensitivity by creating an additional model run, where we switch off the O quenching term in Eq. (1) and compare the resulting $\Delta Z_{9,5}$ values between both model runs. This is done in Fig. 4, where panel (a) shows resulting vertical shifts from a model run including all quenching rate terms in Eq. (2) and panel (b) shows the result for the same model run with deactivated O quenching. Vertical shifts according to weighted peak altitudes are denoted with the solid line, the dotted line denotes vertical shifts based on peak altitudes shifted by the determined HWHM. To visualise the effect of the deactivation of O quenching, we show the difference between both model runs in panel (c). In addition, we also show the difference

ACPD
14, 1239–1285, 2014

between a model run including all quenching rate terms and a model run with deactivated O_2 quenching in panel (d). Because of its rather inefficient quenching capability, we skip a similar comparison for the N_2 quenching.

For the full quenching case, we can find a local maximum in vertical shifts close to −1 h LST in panel (a) of Fig. 4. This maximum is significantly enhanced for the HWHM shifted peak altitudes. If we switch off the O quenching, we can clearly see that vertical shifts have noticeably decreased for both altitude definitions according to panel (b). However, certain similarities persist with respect to the full quenching model run.

For peak shifts calculated from weighted peak altitudes, we can still find a local maximum close to −1 h, which decrease by about 330 m until +5 h. By comparison, the decrease is about 630 m for the full quenching case, i.e. the diurnal decrease in peak shifts increases by a factor of about 1.9 due to the activated O quenching. Interestingly, the deactivation of O_2 quenching is also significantly affecting the peak shifts according to panel (d). However, despite the change of peak shifts by up to 580 m due to the deactivation of O_2 quenching according to panel (d), the difference to the full quenching model run varies only by about 50 m between −1 h and +5 h, which is rather small compared to the effect of O quenching.

For the HWHM shifted peak altitudes, the differences are generally larger when switching the O quenching on and off. Moreover, the response to O quenching in Fig. 4c is less coherent with the diurnal evolution of vertical shifts without O quenching in Fig. 4b. For early (< −3 h) and late (> +3 h) LST, the trend is opposite in both cases. In addition, the strongest impact from O quenching is shifted from −1 h to +1 h LST. This indicates a potential difficulty for our attempt to correlate the diurnal evolution in vertical shifts with that of atomic oxygen, because the diurnal variability of about 670 m in Fig. 4b is very close to the diurnal variability of about 790 m in Fig. 4c, hence we fail to differentiate between the process of O quenching and other processes in Fig. 4b because of their similar magnitudes. Another difficulty arises with respect to O_2 quenching according to Fig. 4d. The activation of O_2 quenching can lead to differences in vertical shifts by up to 1000 m, which again is quite significant. Even though its nighttime

ACPD
14, 1239–1285, 2014

variability is rather constant in the periods between −2 h to +1 h and +3 h to +5 h, the decrease in vertical shifts between these periods is about 650 m, which is significantly larger than for O quenching during the same period.

Keeping in mind the revealed difficulties in our attempt to relate vertical shifts with O quenching, we also have to address the actual method to determine the strength of O quenching. The simplest method is to look at the diurnal evolution of O at a constant height level. However, this method neglects any changes of O concentrations that arise from the vertical motion of the entire OH* layer. To account for this, we may determine the O concentration at a fixed reference point of the OH* layer. Again, this method is still rather simple, because the O quenching is not constrained to a fixed point at the OH* layer. Similar to our example in Fig. 3, we may account for the entire quenching of OH* with O by weighting the vertical O profile with the OH* profile. From all of these approaches, we present their diurnal evolutions in Fig. 5. In addition, we also included the corresponding diurnal evolution of molecular oxygen in the same figure. To allow a better comparison between different methods, we subtracted the minimum value of each curve and denote their values in the legend. If we neglect these offsets, we can still see noticeable differences between different methods, hence the selection between these approaches can lead to different correlations with observed vertical shifts.

For atomic oxygen, we find a single maximum close to −1 h LST according to the fixed 0.241 Pa pressure level (approx. 90 km altitude). If we neglect the −5 h LST, which is close to twilight conditions, O concentrations seem to follow peak shifts based on weighted peak altitudes in panel (c) of Fig. 4. However, the observed response at +1 h for HWHM shifted peak altitudes is not reflected at a constant pressure level. If we interpolate O concentrations at a fixed point of the OH* layer, we find an additional diurnal response around +1 h LST. Although this matches the observed response in vertical shifts based on HWHM shifted peak altitudes in panel (c) of Fig. 4, it is not as pronounced. This situation also remains, if we consider weighted O concentrations.

For molecular oxygen, we find two different situations. On the one hand O_2 concentrations interpolated at weighted peak altitudes and O_2 concentrations weighted with

ACPD
14, 1239–1285, 2014

the OH(9)/OH(5) profiles show a systematic decrease over the course of the night. Moreover, the diurnal gradient is steeper with respect to the lower OH(5) layer. On the other hand, the diurnal variability of O_2 concentrations interpolated at HWHM shifted positions (red lines) is relatively small. In addition, the diurnal variability of O_2 at the 0.241 Pa level is also relatively small. Apparently, the observed larger magnitude of diurnal O_2 changes according to the first two definitions must be connected to the increasing O_2 concentrations with decreasing altitudes. By comparison with the diurnal variability of vertical shifts according to panel (d) of Fig. 4, the systematic decrease with respect to weighted peak altitudes is accompanying the diurnal decrease of O_2 concentrations according to the first two definitions. However, none of our O_2 concentration definitions is capable of reflecting the drastic changes in vertical shifts based on HWHM shifted peak altitudes according to panel (d) of Fig. 4.

In addition to our example close to solstice conditions, we also performed similar tests with respect to equinox conditions, where the amplitude of the migrating diurnal tide maximises. However, despite the larger diurnal variability in O abundances, we encounter similar problems to relate changes in peak shifts with changes of the O and O_2 quenching species.

So far we must conclude that we cannot explain the diurnal variability in vertical shifts between the OH(9)/OH(5) layers with the diurnal variation of the two most important quenching species only. In particular this applies for vertical shifts calculated from HWHM shifted peak altitudes, despite the more pronounced vertical spread between different vibrational populations at this part. In this context we must note that the latter definition is more sensitive to changes in the profile shape of both vertical OH(v) populations. While changes in the profile shape can be induced via modulating the abundances of quenching species, the variability of the $H + O_3$ profiles according to Eq. (2) is also affecting the general OH* profile shape. To account for this additional factor, we therefore extracted the diurnal variation of peak layer FWHM values in Fig. 6. If we consider the difference between the diurnal evolution of OH(9) and OH(5) FWHM values, which corresponds to the black solid line in Fig. 6, we find significantly

ACPD
14, 1239–1285, 2014

CC BY

pronounced changes with a largest difference between both FWHM values around +1 h LST. According to panels (c) and (d) of Fig. 4, the largest response to HWHM shifted peak altitudes appears at the same time, indicating the sensitivity of this parameter to relative changes of peak layer widths.

In addition to this equatorial example, we briefly do a similar comparison for the latitudinal range between 30° N and 60° N, which encloses the strong enhancement of atomic oxygen in the second half of the night. Similar to Fig. 4, different model runs are shown in Fig. 7. As expected, we can see a strong increase of nighttime O for all definitions according to panel (e) of Fig. 7. This time, it is rather the peak shift based on HWHM shifted peak altitudes, which seems to follow the nighttime trend in atomic oxygen. According to Fig. 8, we find again a strong coherence with the relative change in OH(9)/OH(5) peak layer widths. With respect to the deactivation of O_2 quenching according to panel (d) of Fig. 7, it is worth noting that the temporal variability based on weighted peak altitudes is about 140 m, which is more than two times larger compared to the equatorial example. If we consider the diurnal evolution of O_2 according to panel (f), different definitions lead to quite different results. Furthermore, all definitions show systematic differences with respect to the temporal evolution of peak shifts based on weighted peak altitudes according to panel (d). For the peak shifts based on HWHM shifted peak altitudes (same panel), we find again some substantial changes when switching off the O_2 quenching. In general the response of the peak definition based on HWHM shifted peak altitudes shows a strong coherence with the diurnal evolution of relative changes in OH(9)/OH(5) peak widths shown in Fig. 8.

3.4 SABER

Before we will discuss the diurnal evolution of vertical VER profiles measured by SABER, we must address two important issues that would affect a direct comparison with our SD-WACCM4 based results. First of all, our monthly SD-WACCM4 based example covers only half of a full yaw-cycle period that is required by SABER for a full LST coverage. Accordingly, we could extend our monthly SD-WACCM4 period to a full

ACPD
14, 1239–1285, 2014

yaw-cycle, but this would also smear out some interesting features shown before, such as the discussed enhanced OH* concentrations at north-eastern latitudes. Furthermore, our conversion from longitudes to LST assumes that any zonal variability reflects a purely time-dependent process. However Xu et al. (2010) found evidence of noticeable non-migrating tides from SABER observations at lower latitudes, which would violate this assumption. It is for these reasons that we do not intend a direct comparison between SABER and SD-WACCM4 in this section, thus, we will mainly focus on the general relationship between vertical shifts between OH* VER profiles measured by the 1.6 and 2.0 µm SABER channels and changes in derived O concentrations.

Figure 9a and c show derived peak shifts and O concentrations for the equatorial region between 0° and 10° N. Similar to our model study, we determined O concentrations based on different methods. Here, we limit our consideration to O concentrations derived at 90 km altitude and O concentrations weighted with the vertical OH* VER profiles according to both SABER channels. As with our model results, the comparison between peak shifts and O concentrations hardly reveal any consistent relationship. The same also applies for the mid-latitudinal example in Fig. 9b and d, which is suggesting again that the diurnal variability of the vertical peak shifts is mainly driven by the diurnal variability of the H and O_3 profiles.

Similar to our model results, we find a strong variability in the diurnal evolution of the OH* peak widths according to Fig. 9e and f. In particular for the equatorial example, the relative changes in peak widths (see panel (c): black solid line) and vertical shifts based on HWHM shifted peak altitudes (see panel (a): dashed line) show a rather coherent variability. This again reflects the sensitivity of the latter parameter to relative changes in the OH* peak layer widths.

ACPD
14, 1239–1285, 2014

4 Seasonal evolution of OH* layer shifts

4.1 Model study

We leave our case example of the previous section and will now focus on the full year period of simulated OH* starting from April 2010. Similar to the previous section, we will investigate to what extent the seasonal variability of $\Delta Z_{9,5}$ peak shifts is affected by the quenching of OH* with molecular and atomic oxygen.

With respect to equatorial latitudes, the diurnal migrating tide is an important process affecting the OH* airglow and ambient temperatures (Shepherd et al., 2006). Many studies have reported evidence of a semi-annual oscillation in airglow observations that is associated with the large seasonal changes in the tidal amplitude. For instance, Marsh et al. (2006) present a pronounced semi-annual oscillation in SABER OH* VER measurements at equatorial latitudes. A similar seasonality was also recently shown for OH* VER measurements from SCIAMACHY (SCanning Imaging Absorption spectroMeter for Atmospheric CHartographY) by von Savigny and Lednyts'kyy (2013). In addition, a semi-annual oscillation was also reported from HRDI observations (Yee et al., 1997) and ISIS-2 observations (Cogger et al., 1981) of the O(^{1}S) green line. Because the vertically integrated O concentration should be proportional to the integrated OH* VER (see Eq. 2 in Mlynczak et al., 2013), the same observed seasonal variability could also apply for the $\Delta Z_{9,5}$ peak shift. Indeed, the study of von Savigny and Lednyts'kyy (2013) finds evidence of the same semi-annual oscillation between SCIAMACHY measurements of O abundances derived from the O(^{1}S) green line and the vertical displacement between the OH(3-1)/OH(6-2) transmission bands at equatorial latitudes.

Following-up these findings, Fig. 10 shows 1 yr of SD-WACCM4 O concentrations together with derived OH(9) concentrations at equatorial latitudes in the LST range from 23:00 to 00:00 UTC. The enhancements in OH* concentrations around both equinoxes confirm the reported enhancements in OH* VER from Marsh et al. (2006) and von Savigny and Lednyts'kyy (2013). A similar annual pattern also exists for OH(5)

ACPD
14, 1239–1285, 2014

concentrations (not shown). In addition, we can find similar enhancements in atomic oxygen around both equinoxes, which again is consistent with the previously suggested proportionality between O and OH* concentrations. Interestingly, a similar semi-annual oscillation also exists for O_2 concentrations according to the lower right panel of Fig. 10 except for O_2 concentrations at the constant 0.241 Pa pressure level. This indicates the important role of the seasonal variability of the effective O_2 quenching process, which in turn can significantly affect the vertical OH* structure according to the previous section.

If we consider the resulting $\Delta Z_{9,5}$ peak shifts based on weighted peak altitudes in Fig. 11, we can also find an enhancement around both equinoxes, but a less distinct minimum close to the December solstice. According to the panel (b) in Fig. 11, the equinoctial enhancements in $\Delta Z_{9,5}$ peak shifts still persist, if we switch off the O quenching, however, the $\Delta Z_{9,5}$ maximum around the December solstice is contrasting the temporal evolution of O concentrations. The semi-annual oscillation in $\Delta Z_{9,5}$ peak shifts is seen more clearly, if we subtract model runs with and without O quenching from each other as shown in panel (c). The comparison between both model runs indicates that the semi-annual amplitudes enhance by a factor of about 2.5, if we consider O quenching in our OH* model. For the deactivation of quenching with O_2, the impact on the seasonal evolution of $\Delta Z_{9,5}$ peak shifts is smaller with respect to weighted peak altitudes according to panel (d). For instance, the peak shift variation between August and October is about 200 m for switching O quenching on and off, which is about two time larger compared to switching the O_2 quenching on and off. With respect to HWHM shifted peak altitudes, again a significant seasonal variability exists in panel (d).

In addition to $\Delta Z_{9,5}$ peak shifts and O concentrations, we find another semi-annual oscillation in the weighted OH* peak altitudes (see panel (e) of Fig. 11) in accordance with other studies (e.g. see Shepherd et al., 2006, and von Savigny and Lednyts'kyy, 2013). Interestingly, this oscillation is in anti-phase to the semi-annual oscillations in O and OH* concentrations. As noted in the previous section, an anti-correlation exists between integrated OH* concentrations and peak altitudes, therefore the observed phase shift is something we would expect from this anti-correlation. Because of the

ACPD
14, 1239–1285, 2014

strong vertical gradient in O concentrations at OH* altitudes, the seasonal variability in OH* peak altitudes induces a semi-annual oscillation that should be associated with stronger O quenching around each solstice. Despite the opposing effect between the vertical and temporal change in O concentrations, the temporal variability appears to dominate the seasonal variability in the O quenching according to Fig. 11. On the other hand, the large enhancement in peak altitudes around January associated with larger O quenching could explain the less distinct minimum in peak shifts around the solstice period. We should note that an anti-phase relation also exists between OH* altitudes and O_2 concentrations. Because of the still relatively constant O_2 VMR at these altitudes, absolute concentrations are modulated via temperature/pressure changes. Interestingly, the anti-phase relation to OH* altitudes rather seems to contribute to the observed semi-annual oscillation in O_2 in contrast to O because of the increasing O_2 density with decreasing altitudes. In addition, the temperature changes due to the modulation of the amplitude of the migrating diurnal tide, is also affecting the absolute O_2 concentrations.

With respect to the HWHM shifted peak altitudes, it is more difficult to find a clear seasonal dependency according to Fig. 11. By subtracting our OH* model runs with and without O quenching from each other, two distinct enhancements remain around both equinoxes. In particular the change in $\Delta Z_{9,5}$ peak shifts from summer-solstice to the mid of October is about two times larger, if we consider shifted instead of weighted peak altitudes. However, these enhancements are almost constrained to a single month each, i.e. they follow a more pulse like response rather than a smooth harmonic oscillation. Again, the comparison with the relative change of peak layer widths according to panel (f) of Fig. 11 shows strong changes during the same months, but also some differences remain with respect to the seasonal variability according to panel (a).

In contrast to the pronounced semi-annual variability at low latitudes, we would expect a dominating annual response, which is associated with the vertical component of the meridional circulation (Marsh et al., 2006). Furthermore, we would expect that this variability should be noticed at all local times, since it is related to the (local time

ACPD
14, 1239–1285, 2014

independent) meridional circulation. However, if we consider the global distribution of vertically integrated OH* in Fig. 2, it is obvious that the nighttime period rapidly decreases during the summer season at high latitudes. Apparently, the inclusion of periods with daytime OH* would introduce a significant annual oscillation in OH* concentrations that is independent of the meridional circulation. Hence, we preferably select a local time within a latitudinal range that is not affected by sunlit photochemistry throughout the year to investigate the influence of the meridional circulation on OH* concentrations. Accordingly, we choose the latitudinal range from 50° S to 55° S at 00:00 UTC in Fig. 12. For the annual variability of atomic oxygen we can see a pronounced maximum in O concentrations at the Northern Hemisphere around January 2011, which is shortly followed by a similar enhancement at the Southern Hemisphere in February 2011. The reported 60° S OH* maximum around May from Marsh et al. (2006) does not fit with the SD-WACCM4 enhancement in O concentration. This could indicate a special case with respect to the vertical transport component of the meridional circulation in 2011, but due to our limited dataset and our general emphasis on O quenching the final assessment of this question already exceeds the scope of this paper.

In contrast to our comparison in Fig. 11, the impact of O (and O_2) quenching seems to play a minor role for the variability in $\Delta Z_{9,5}$ peak shifts at higher latitudes. This result might be surprising, in particular when considering the relatively constrained periods with high O concentrations in both hemispheres. With respect to weighted peak altitudes, the response in $\Delta Z_{9,5}$ peak shifts to changes in O concentrations only becomes visible when subtracting the model runs with and without O quenching from each other. For instance, we can find two enhancements in $\Delta Z_{9,5}$ peak shifts in November and February and a minimum around August in the SH, which fits to the seasonal change in O concentrations according to Fig. 12. However, the seasonal variability in $\Delta Z_{9,5}$ peak shifts is ranging with the same magnitude, if we switch off the O quenching. For the $\Delta Z_{9,5}$ peak shifts based on HWHM shifted peak altitudes the coherency with the seasonal variability of O concentrations is less satisfactory. Again, this peak shift

ACPD
14, 1239–1285, 2014

definition appears to be highly affected by the relative change of peak layer widths, showing a semi-annual oscillation around both equinox.

4.2 Comparison with SABER

We will now focus on the seasonal variability of the vertical shifts between OH* profiles according to SABER VER measurements within the same −1 h to 0 h LST bin that is also used for our model study. Figure 14 shows the seasonal variability of equatorial OH* peak shifts and O concentrations, that are both derived from VER measurements of the SABER 1.6 and 2.0 µm channels for the period from January 2009 to December 2011. Figure 15 gives a similar example for high latitudes.

By comparing both equatorial latitude bins, a semi-annual oscillation in OH* weighted O concentrations is much more pronounced for the 0° to 10° S bin than for the 0° to 10° N bin, where an apparent annual component dominates. A similar situation applies for the O concentrations at 90 km altitude. Interestingly, a pronounced semi-annual oscillation is apparent for both equatorial latitude bins in terms of peak shifts between both OH* SABER profiles. Even though the semi-annual amplitude of peak shifts based on weighted peak altitudes is larger for the 0° to 10° S bin, it is worth noting that a semi-annual oscillation persists for the 0° to 10° N latitude bin despite the dominating annual component of the corresponding atomic oxygen oscillation. This again indicates that further processes must be taken into account for the seasonal variation of OH* peak shifts. Furthermore, the strong coherence between the relative modulation of VER profile widths and peak shifts based on shifted peak altitudes (compare dashed line of upper panels with solid black line of lower panels) confirms the strong relationship between both parameters that has also been previously observed in this study.

The mid-latitudinal example in Fig. 15 is rather dominated by an annual oscillation through all parameters. In particular the relative change between the VER profile widths observed from both SABER channels shows a strongly coherent annual oscillation, while the results based on SD-WACCM4 simulations show a semi-annual oscillation. Moreover, in contrast to the simulated SD-WACCM4 O concentrations, we cannot find

ACPD
14, 1239–1285, 2014

a similar strong increase shortly after the turn over of the meridional circulation in February for the SABER observations. However, the larger averaging time due to our constraint of one yaw cycle could smooth out such an event.

5 Summary and conclusion

By combining a quenching model with a state-of-the-art 3-D chemical climate model (SD-WACCM4), this study has investigated the temporal evolution of the OH* species with special emphasis on the impact of the quenching process due to O and O_2. Based on a monthly case example, this model approach confirms general features of the global distribution of OH* that have been reported by previous observational and theoretical studies, in summary:

- The diurnal decrease in nighttime OH* concentrations.
- The inverse relationship between integrated OH* columns and OH* peak altitudes.
- The prominence of single peak OH* profiles during nighttime.

The latter point suggests that complex structures, which have been observed in vertical OH* VER profiles during nighttimes, are caused more likely by lateral rather than vertical inhomogeneities in the distribution of OH*.

Even though, the main focus of this study is on the nighttime, some interesting SD-WACCM4 based daytime features were revealed in addition, i.e.:

- Daily profiles show more complex structures.
- Pronounced synoptic scale features of large daytime OH* abundances exist.

While the first point confirms the impact of higher daytime abundances of H on the production of OH*, the latter point is quite surprising for us, because OH* daytime

ACPD
14, 1239–1285, 2014

abundances are significantly affected by sunlit photochemistry. Moreover, these features are most prominent during solstice conditions and mainly constrained to summer hemispheric mid-latitudes. A further investigation of these systematic features is needed.

In the next part of this study, the quenching of OH* with O and O_2 was investigated by creating model runs with:

- Full quenching.
- Deactivated O quenching.
- Deactivated O_2 quenching.

From these model runs, vertical displacements between the OH(9) and OH(5) layers are determined and compared with abundances of the O and O_2 quenching species. We find that despite the deactivation of O and O_2 quenching, a noticeable temporal variability remains in the vertical OH(9)/OH(5) displacements in both cases, which must be attributed to the natural variability in the H and O_3 profiles that lead to the production of OH*. For the diurnal variability, this factor is even dominating in both, SD-WACCM4 based simulations and SABER observations, hence we fail to find a significant correlation between the vertical OH(9)/OH(5) displacements and the effective quenching with either O or O_2. However, the situation has changed for the seasonal evolution at the equatorial regions. In this case, a pronounced semi-annual oscillation exists in the vertical displacement of the simulated OH(9)/OH(5) layers, which we also find in the OH* VER measurements from SABER. In addition, our study reveals that a similar oscillation also exists for the absolute O and O_2 concentrations at OH* layer altitudes, thus, demonstrating the importance of the quenching process to the revealed semi-annual oscillation in the vertical OH* profile structure. While previous studies have already outlined the effect of O quenching to the OH* profile, the systematic impact of O_2 quenching on the vertical OH* structure is, to our knowledge, a new aspect in terms of the processes that are driving the semi-annual response in OH* airglow (e.g. see

ACPD
14, 1239–1285, 2014

Gattinger et al., 2013 and references therein). In general, despite the less efficient O_2 quenching compared to O quenching, we must conclude from our study, that the higher absolute abundance of O_2 is compensating this, in particular at the lower part of the OH* layer.

In addition to the semi-annual oscillation of the two most important OH* quenching species, we also find a remaining similar oscillation in the model runs with deactivated quenching parameters. This implies that the natural variability of H and O_3 still plays a noticeable role for the seasonal variability of the vertical OH* structure. Therefore, we conclude from our model results that the observed semi-annual oscillation cannot be entirely explained by the quenching process alone.

Because of the manifold of transition bands being observed by different ground-based instruments, a thorough understanding of the driving processes of the variability of OH* emission altitudes is crucial for the intercomparison and interpretation of long-term data sets. This in particular applies for the studying of mesopause temperature trends by means of OH* rotational temperature measurements (see Beig et al., 2003; Beig, 2011, for a comprehensive review on this topic). A future model study, which includes a multiyear analysis of the features that have been discussed here, would further contribute to a better quantitative understanding of the systematic biases between different observational long-term studies.

Acknowledgements. This work was in part supported by the Ernst-Moritz-Arndt-University of Greifswald. Further support was granted by the German Research Foundation (Deutsche Forschungsgemeinschaft, DFG) under project PA 1714/4-2. We thank I. McDade, York University, Toronto, for the provision of the initial quenching algorithm, which we have adapted in the frame of this study. We also thank R. R. Garcia and D. E. Kinnison, NCAR Boulder, for providing the SD-WACCM4 data to us, which have been a crucial component of this study. In addition, we thank C. Hoffman, former member of the IUP Bremen and A. K. Smith, NCAR Boulder, for the helpful discussions on the SD-WACCM4 data and the employed quenching model to this study. Finally, we are indebted to the SABER team for making SABER data available.

References

Adler-Golden, S.: Kinetic parameters for OH nightglow modeling consistent with recent laboratory measurements, J. Geophys. Res., 102, 19969–19976, 1997. 1241, 1270

Bates, D. R. and Nicolet, M.: The photochemistry of atmospheric water vapor, J. Geophys. Res., 55, 301–327, 1950. 1241

Beig, G.: Long-term trends in the temperature of the mesosphere/lower thermosphere region: 2. Solar response, J. Geophys. Res., 116, A00H12, doi:10.1029/2011JA016766, 2011. 1265

Beig, G., Keckhut, P., Lowe, R. P., Roble, R. G., Mlynczak, M. G., Scheer, J., Fomichev, V. I., Offermann, D., French, W. J. R., Shepherd, M. G., Semenov, A. I., Remsberg, E. E., She, C. Y., Lübken, F. J., Bremer, J., Clemesha, B. R., Stegman, J., Sigernes, F., and Fadnavis, S.: Review of mesospheric temperature trends, Rev. Geophys., 41, 1015–1055, doi:10.1029/2002RG000121, 2003. 1265

Cho, Y.-M. and Shepherd, G.: Correlation of airglow temperature and emission rate at Resolute Bay (74.86° N), over four winters (2001–2005), Geophys. Res. Lett., 33, L06815, doi:10.1029/2005GL025298, 2006. 1249

Cogger, L. L., Elphinstone, R. D., and Murphree, J. S.: Temporal and latitudinal 5577 A airglow variations, Can. J. Phys., 59, 1296–1307, 1981. 1258

Dodd, J. A., Lipson, S. J., Lowell, J. R., Armstrong, P. S., Blumberg, W. A. M., Nadile, R. M., Adler-Golden, S. M., Marinelli, W. J., Holtzclaw, K. W., and Green, B. D.: Analysis of hydroxyl earthlimb airglow emissions: kinetic model for state-to-state dynamics of OH (v,N), J. Geophys. Res., 99, 3559–3585, 1994. 1241

Funke, B., López-Puertas, M., García-Comas, M., Kaufmann, M., Höpfner, M., and Stiller, G.: GRANADA: a Generic RAdiative traNsfer AnD non-LTE population Algorithm, J. Quant. Spectrosc. Ra., 113, 1771–1817, 2012. 1248

Garcia, R. R., Marsh, D. R., Kinnison, D. E., Boville, B. A., and Sassi, F.: Simulation of secular trends in the middle atmosphere, 1950; 2003, J. Geophys. Res., 112, D09301, doi:10.1029/2006JD007485, 2007. 1245

Gattinger, R. L., Kyrölä, E., Boone, C. D., Evans, W. F. J., Walker, K. A., McDade, I. C., Bernath, P. F., and Llewellyn, E. J.: The roles of vertical advection and eddy diffusion in the equatorial mesospheric semi-annual oscillation (MSAO), Atmos. Chem. Phys., 13, 7813–7824, doi:10.5194/acp-13-7813-2013, 2013. 1265

ACPD
14, 1239–1285, 2014

Hoffmann, C. G., Kinnison, D. E., Garcia, R. R., Palm, M., Notholt, J., Raffalski, U., and Hochschild, G.: CO at 40–80 km above Kiruna observed by the ground-based microwave radiometer KIMRA and simulated by the Whole Atmosphere Community Climate Model, Atmos. Chem. Phys., 12, 3261–3271, doi:10.5194/acp-12-3261-2012, 2012. 1245

Khomich, V., Semenov, A., and Shefov, N.: Airglow as an Indicator of Upper Atmospheric Structure and Dynamics, Springer, Berlin, Heidelberg, 2008. 1244, 1247

Krassovsky, V. I.: Chemistry of the upper atmosphere, Space Res., 3, 96–116, 1963. 1244

Liu, G. and Shepherd, G. G.: An empirical model for the altitude of the OH nightglow emission, Geophys. Res. Lett., 33, L09805, doi:10.1029/2005GL025297, 2006. 1249

Makhlouf, U. B., Picard, R. H., and Winick, J. R.: Photochemical-dynamical modeling of the measured response of airglow to gravity waves 1. Basic model for OH airglow, J. Geophys. Res., 100, 11289–11311, 1995. 1241

Marsh, D. R., Smith, A. K., Mlynczak, M. G., and Russell, J. M.: SABER observations of the OH Meinel airglow variability near the mesopause, J. Geophys. Res., 111, A10S05, doi:10.1029/2005JA011451, 2006. 1242, 1249, 1258, 1260, 1261

McDade, I. C.: The altitude dependence of the OH($X^2\Pi$) vibrational distribution in the nightglow: some model expectations, Planet. Space Sci., 39, 1049–1057, 1991. 1241, 1243, 1244

McDade, I. C. and Llewellyn, E. J.: Mesospheric oxygen atom densities inferred from night-time OH Meinel band emission rates, Planet. Space Sci., 36, 897–905, 1988. 1243

Melo, S. M. L., Lowe, R. P., and Russell, J. P.: Double-peaked hydroxyl airglow profiles observed from WINDII/UARS, J. Geophys. Res., 105, 12397–12403, 2000. 1250

Mertens, C. J., Russell III, J. M., Mlynczak, M. G., She, C.-Y., Schmidlin, F. J., Goldberg, R. A., López-Puertas, M., Wintersteiner, P. P., Picard, R. H., Winick, J. R., and Xu, X.: Kinetic temperature and carbon dioxide from broadband infrared limb emission measurements taken from the TIMED/SABER instrument, Adv. Space. Res., 43, 15–27, 2009. 1247

Mlynczak, M. G., Hunt, L. A., Mast, J. C., Thomas Marshall, B., Russell, J. M., Smith, A. K., Siskind, D. E., Yee, J.-H., Mertens, C. J., Javier Martin-Torres, F., Earl Thompson, R., Drob, D. P., and Gordley, L. L.: Atomic oxygen in the mesosphere and lower thermosphere derived from SABER: algorithm theoretical basis and measurement uncertainty, J. Geophys. Res.-Atmos., 118, 5724–5735, 2013. 1247, 1258

Rothman, L., Gordon, I., Barbe, A., Benner, D., Bernath, P., Birk, M., Boudon, V., Brown, L., Campargue, A., Champion, J.-P., Chance, K., Coudert, L., Dana, V., Devi, V., Fally, S., Flaud, J.-M., Gamache, R., Goldman, A., Jacquemart, D., Kleiner, I., Lacome, N., Lafferty, W.,

Mandin, J.-Y., Massie, S., Mikhailenko, S., Miller, C., Moazzen-Ahmadi, N., Naumenko, O., Nikitin, A., Orphal, J., Perevalov, V., Perrin, A., Predoi-Cross, A., Rinsland, C., Rotger, M., Šimečková, M., Smith, M., Sung, K., Tashkun, S., Tennyson, J., Toth, R., Vandaele, A., and Vander Auwera, J.: The HITRAN 2008 molecular spectroscopic database, J. Quant. Spectrosc. Ra., 110, 533–572, 2009. 1270

Russell III, J. M., Mlynczak, M. G., Gordley, L. L., Tansock Jr., J. J., and Esplin, R. W.: Overview of the SABER experiment and preliminary calibration results, in: Soc. Photo-Opt. Instru. (SPIE) Conference Series, edited by: Larar, A. M., Proc. SPIE 3756, Optical Spectroscopic Techniques and Instrumentation for Atmospheric and Space Research III, 277–288, doi:10.1117/12.366382, 1999. 1246

Sander, S. P., Abbatt, J., Barker, J. R., Burkholder, J. B., Friedl, R. R., Golden, D. M., Huie, R. E., Kolb, C. E., Kurylo, M. J., Moortgat, G. K., Orkin, V. L., and Wine, P. H.: Chemical Kinetics and Photochemical Data for Use in Atmospheric Studies, Evaluation No. 17, JPL Publication, Jet Propulsion Laboratory, Pasadena, 10–66, 1–12, 2011. 1270

Shepherd, M. G., Liu, G., and Shepherd, G. G.: Mesospheric semiannual oscillation in temperature and nightglow emission, J. Atmos. Sol.-Terr. Phy., 68, 379–389, 2006. 1258, 1259

Smith, A. K., Marsh, D. R., Mlynczak, M. G., and Mast, J. C.: Temporal variations of atomic oxygen in the upper mesosphere from SABER, J. Geophys. Res., 115, D18309, doi:10.1029/2009JD013434, 2010. 1270

Smith, A. K., Garcia, R. R., Marsh, D. R., and Richter, J. H.: WACCM simulations of the mean circulation and trace species transport in the winter mesosphere, J. Geophys. Res., 116, D20115, doi:10.1029/2011JD016083, 2011. 1252

Steinfeld, J. I., Adler-Golden, S. M., and Gallagher, J. W.: Critical survey of data on the spectroscopy and kinetics of ozone in the mesosphere and thermosphere, Phys. Chem. Ref. Data, 16, 911–951, 1987. 1270

von Savigny, C. and Lednyts'kyy, O.: On the relationship between atomic oxygen and vertical shifts between OH Meinel bands originating from different vibrational levels., Geophys. Res. Lett., 40, 5821–5825, doi:10.1002/2013GL058017, 2013. 1241, 1258, 1259

von Savigny, C., McDade, I. C., Eichmann, K.-U., and Burrows, J. P.: On the dependence of the OH* Meinel emission altitude on vibrational level: SCIAMACHY observations and model simulations, Atmos. Chem. Phys., 12, 8813–8828, doi:10.5194/acp-12-8813-2012, 2012. 1241, 1243, 1244, 1247

Xu, J., Smith, A. K., Jiang, G., Gao, H., Wei, Y., Mlynczak, M. G., and Russell, J. M.: Strong longitudinal variations in the OH nightglow, Geophys. Res. Lett., 37, L21801, doi:10.1029/2010GL043972, 2010. 1257

Xu, J., Gao, H., Smith, A. K., and Zhu, Y.: Using TIMED/SABER nightglow observations to investigate hydroxyl emission mechanisms in the mesopause region, J. Geophys. Res., 117, D02301, doi:10.1029/2011JD016342, 2012. 1244, 1270

Yee, J.-H., Crowley, G., Roble, R. G., Skinner, W. R., Burrage, M. D., and Hays, P. B.: Global simulations and observations of O(1S), O2(1SIGMA) and OH mesospheric nightglow emissions, J. Geophys. Res., 102, 19949–19968, 1997. 1258

ACPD
14, 1239–1285, 2014

Table 1. Employed constants to Eq. (2).

constant	reference	remark
P	Adler-Golden (1997)	based on values from Steinfeld et al. (1987)
A	Xu et al. (2012)	values based on Hitran database (Rothman et al., 2009)
$k_3^{O_2}$; α	Adler-Golden (1997)	based on Table 2; α = correction factor from Xu et al. (2012)
$k_L^{N_2}$	Adler-Golden (1997)	taken from Table 1
k_L^{O} ; β	Smith et al. (2010)	β = correction factor from Xu et al. (2012)
k_1	Sander et al. (2011)	

ACPD
14, 1239–1285, 2014

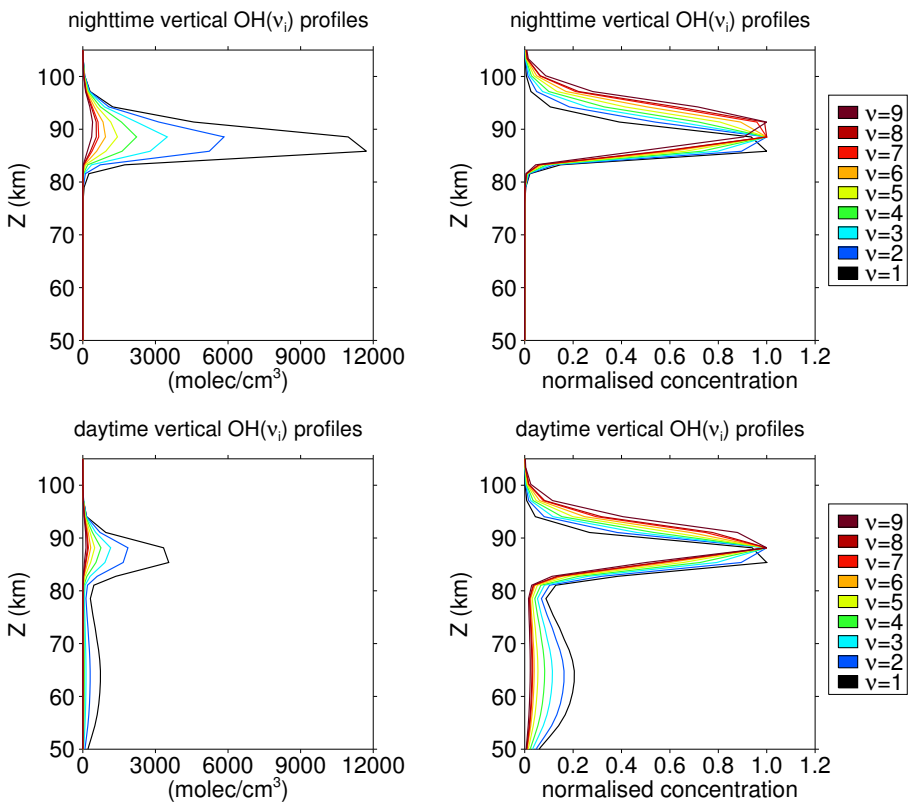

Fig. 1. Vertical OH(ν) profiles calculated from SD-WACCM4 model output. The profiles correspond to a monthly average in January 2011 at 45° S, with upper panels referring to a nighttime example at 0° longitude and lower panels referring to a daytime example at 90° W. Absolute concentrations are shown on the left panels, concentrations normalised to the maximum value of each vibrational population are shown on the right panels.

ACPD
14, 1239–1285, 2014

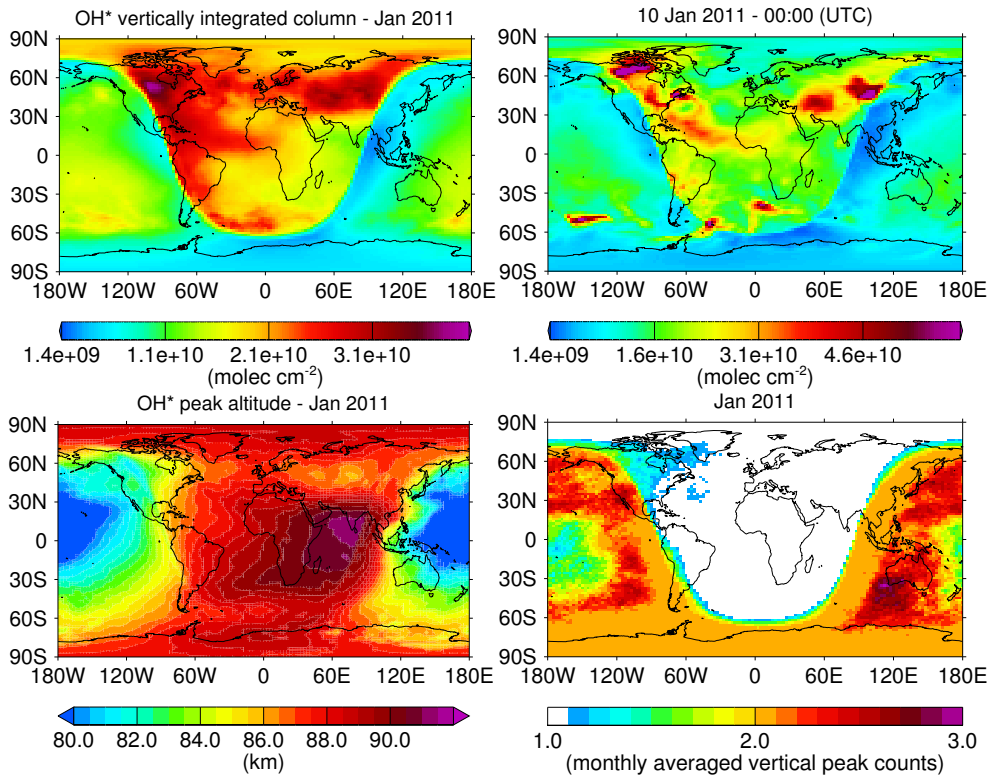

Fig. 2. Upper panels: vertically integrated number density of simulated $\sum_{i=1}^{9} \mathrm{OH}(v_i)$, (left) monthly averaged data from 00:00 UTC daily results, (right) daily snapshot. Lower panels: monthly average of determined peak altitudes weighted with OH* concentrations (left), monthly averaged counts of detected multiple peak numbers of vertical OH* profiles (right).

ACPD
14, 1239–1285, 2014

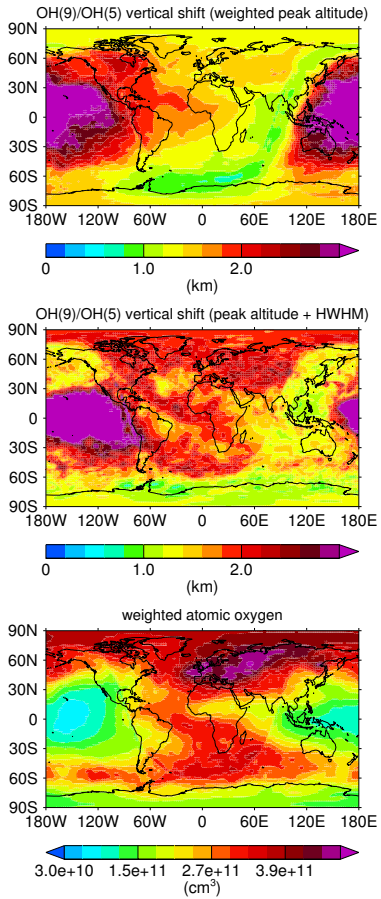

Fig. 3. Same monthly average as shown in Fig. 2. Vertical displacement $\Delta Z_{9,5}$ between OH(9)/OH(5) weighted peak altitudes (upper panel) and OH(9)/OH(5) peak altitudes at HWHM (middle panel). Lower panel: SD-WACCM4 O concentration weighted with vertical OH(9) profiles.

ACPD
14, 1239–1285, 2014

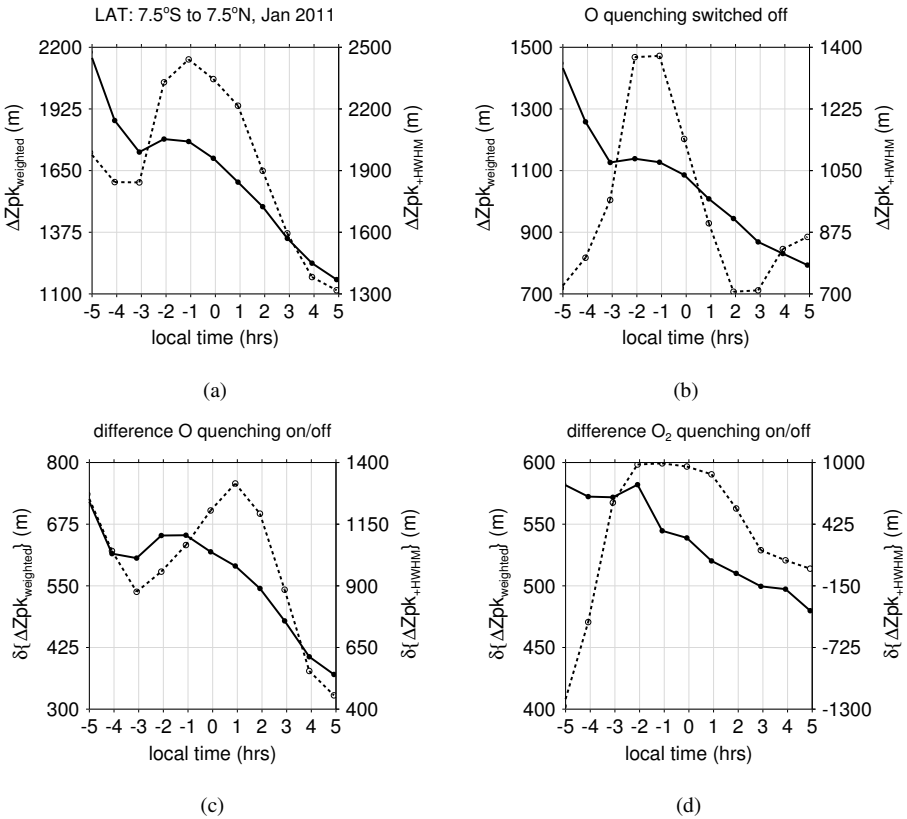

Fig. 4. Diurnal evolution of vertical shifts at equatorial latitudes. Panel **(a)**: vertical shifts based on a model run including all quenching terms. The solid line refers to peak shifts with respect to weighted peak altitudes, the dashed line refers to vertical shifts with respect to peak altitudes + HWHM. Panel **(b)**: peak shifts based on a model run with deactivated O quenching. Panel **(c)**: difference between panel (**a** and **b**). Panel **(d)**: difference between a full quenching model run and a model run with deactivated O_2 quenching.

ACPD
14, 1239–1285, 2014

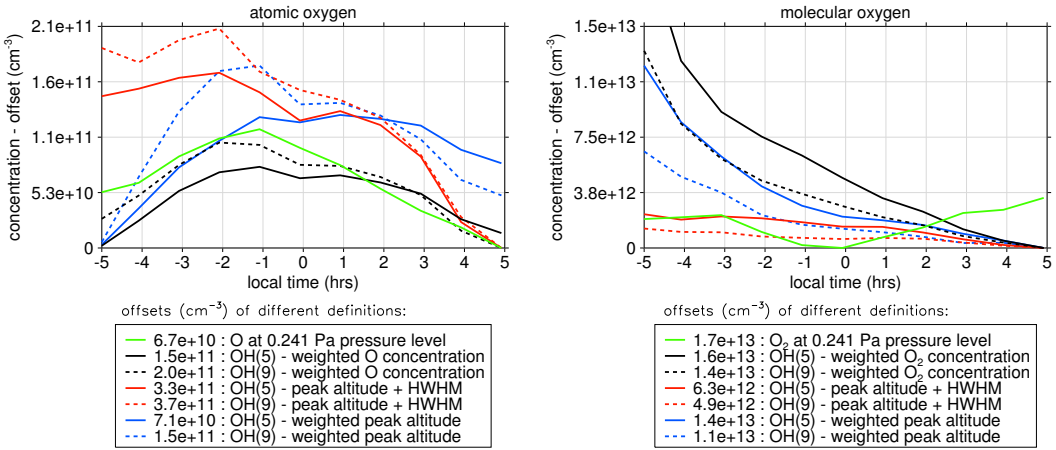

Fig. 5. Diurnal variability of atomic and molecular oxygen sensed according to 4 different approaches: O concentration at fixed pressure level (green line), O concentration interpolated at shifted and weighted peak altitudes (red and blue lines), O concentration weighted with OH* concentrations (black lines). From each curve the offsets listed in the legend were subtracted to allow a better comparison.

ACPD
14, 1239–1285, 2014

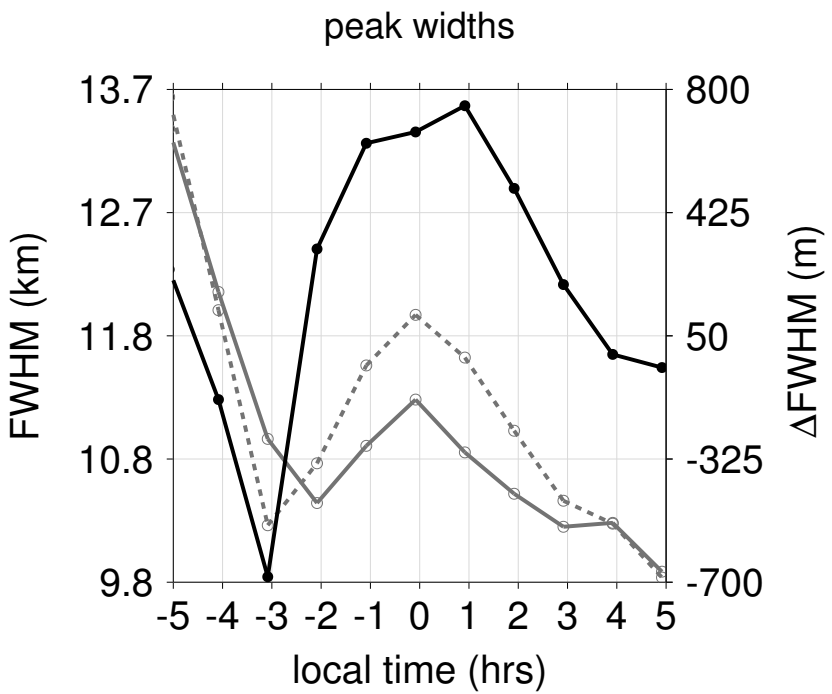

Fig. 6. Diurnal variability of FWHM of OH(9) layer (grey dashed line) and OH(5) layer (grey solid line) based on the full quenching model run according to Fig. 4a. The difference ΔFWHM between both lines is denoted by the black solid line.

ACPD
14, 1239–1285, 2014

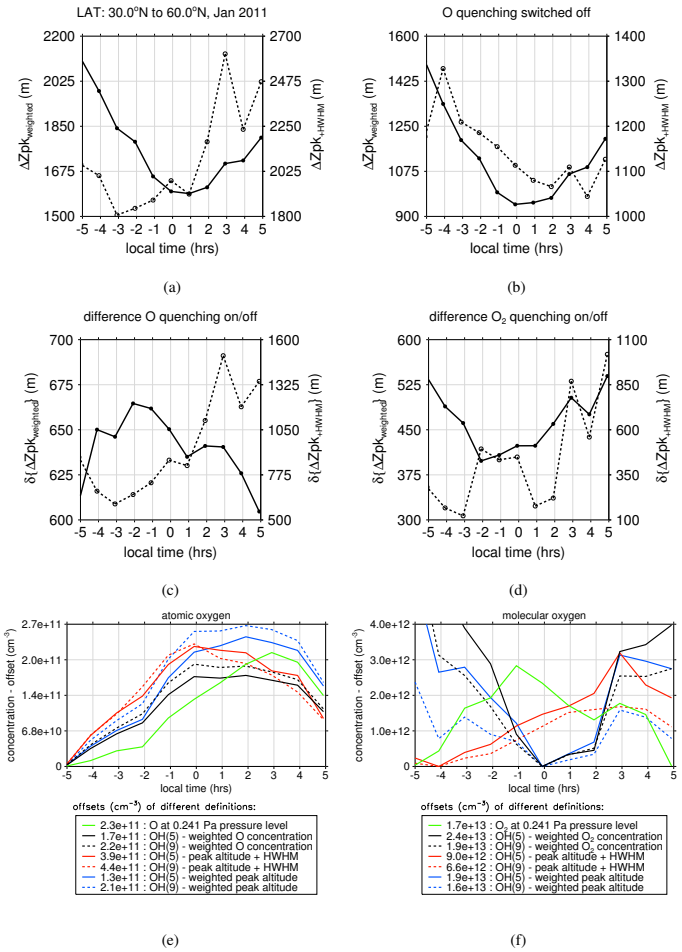

Fig. 7. Similar to plots shown in Figs. 4 and 5, but referring to the latitudinal range between 30° N and 60° N.

ACPD
14, 1239–1285, 2014

CC BY

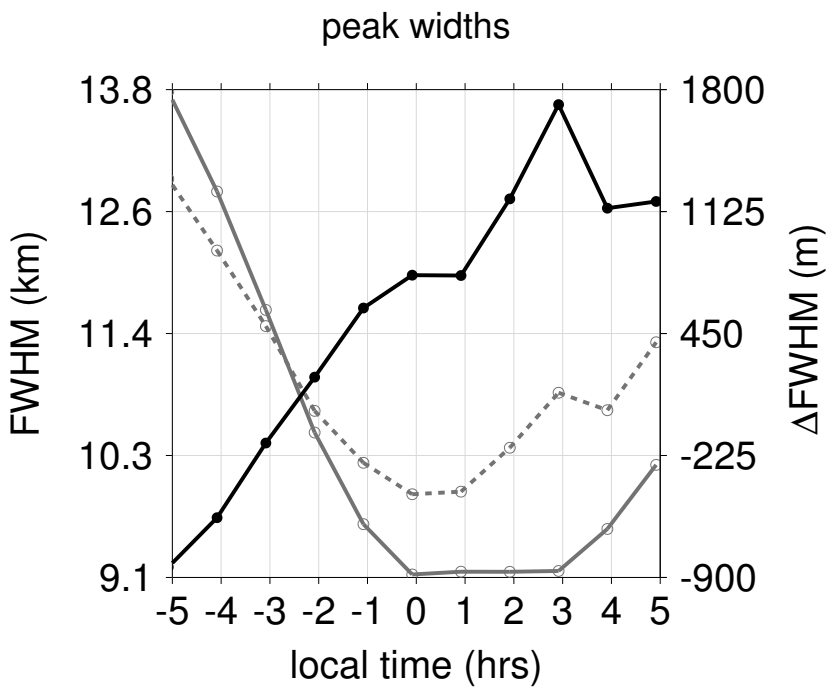

Fig. 8. Similar to Fig. 6 but with respect to the 30° N to 60° N latitude bin.

ACPD
14, 1239–1285, 2014

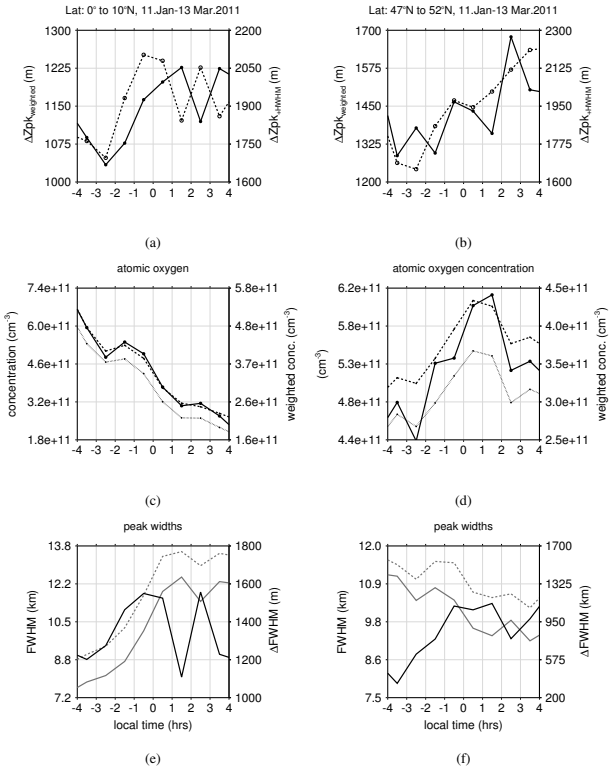

Fig. 9. Diurnal variability at the equator (left panels) and high latitudes (right panels) according to VER measurements from SABER: **(a** and **b)** peak shift based on weighted peak altitudes (solid lines) and peak altitudes + HWHM (dashed lines). **(c** and **d)** atomic oxygen weighted with OH radiance from the 1.6 µm channel (dotted line), the 2.0 µm (dashed line) and number density at 90 km altitude (solid line). **(e** and **f)** FWHM of 1.6 µm vertical VER profile (grey dashed line), FWHM of 2.0 µm vertical VER profile (grey solid line), and the difference ΔFWHM between both FWHM values (black solid line).

ACPD
14, 1239–1285, 2014

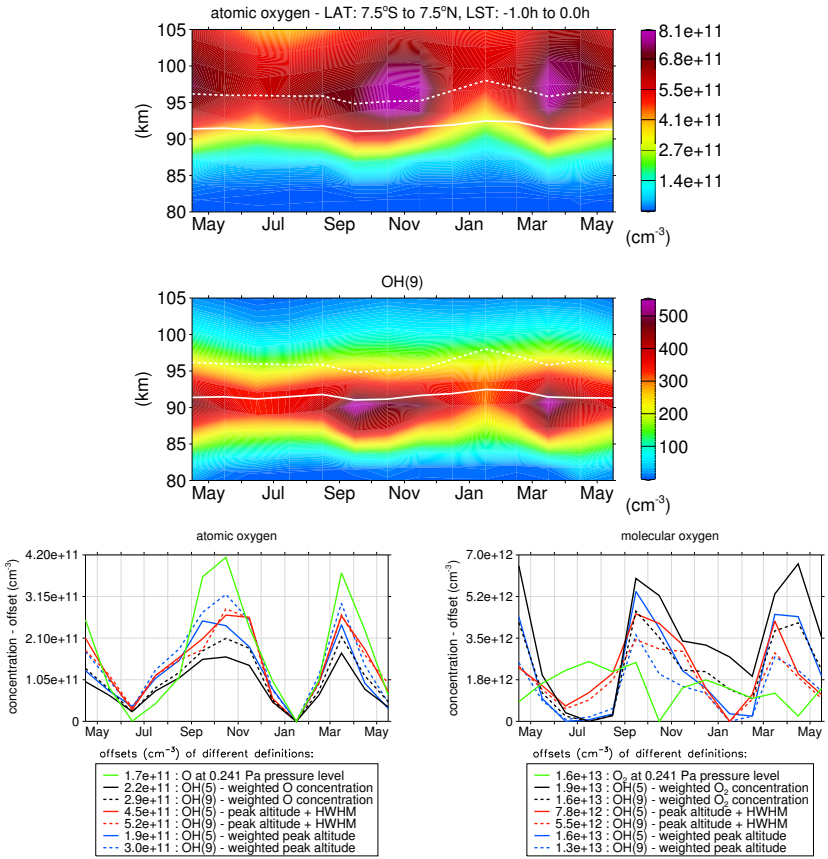

Fig. 10. Upper and middle panels: Seasonal variability of O and OH(9) concentrations covering the period from mid-April 2010 to mid-May 2011 based on monthly averages. Weighted OH(9) peak altitudes are denoted by the solid white line in both panels, OH(9) peak altitudes + HWHM are denoted by the dashed white line. Lower panels: corresponding seasonal variability of atomic and molecular oxygen similar to Fig. 5.

ACPD
14, 1239–1285, 2014

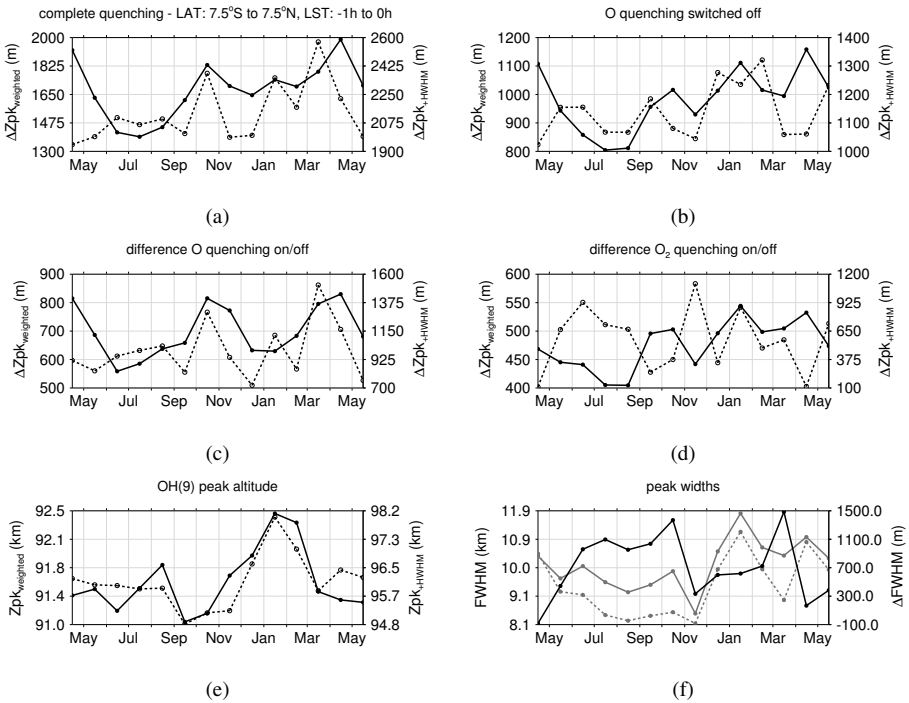

Fig. 11. Panel **(a–d)**: seasonal variability of OH peak shifts for different model runs within the equatorial range between ±7.5° similar to those presented in panel **(a–d)** of Fig. 4. Panel **(e)**: weighted OH(9) peak altitudes (solid line) and OH(9) peak altitudes + HWHM (doted lines). Panel **(f)**: peak widths according to the same annotation as used in Fig. 6.

ACPD
14, 1239–1285, 2014

CC BY

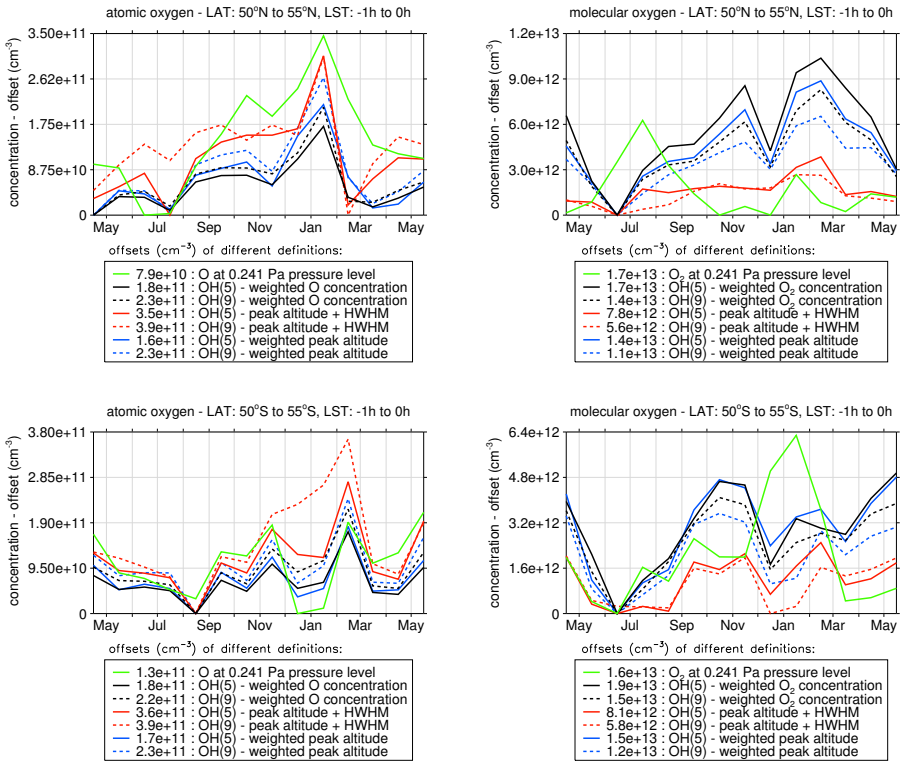

Fig. 12. Seasonal variability of O and O_2 concentrations at OH* altitudes according to the −1 h to +1 h LST bin and a 50° to 55° latitudinal bin: upper panels Northern Hemisphere, lower panels Southern Hemisphere.

ACPD
14, 1239–1285, 2014

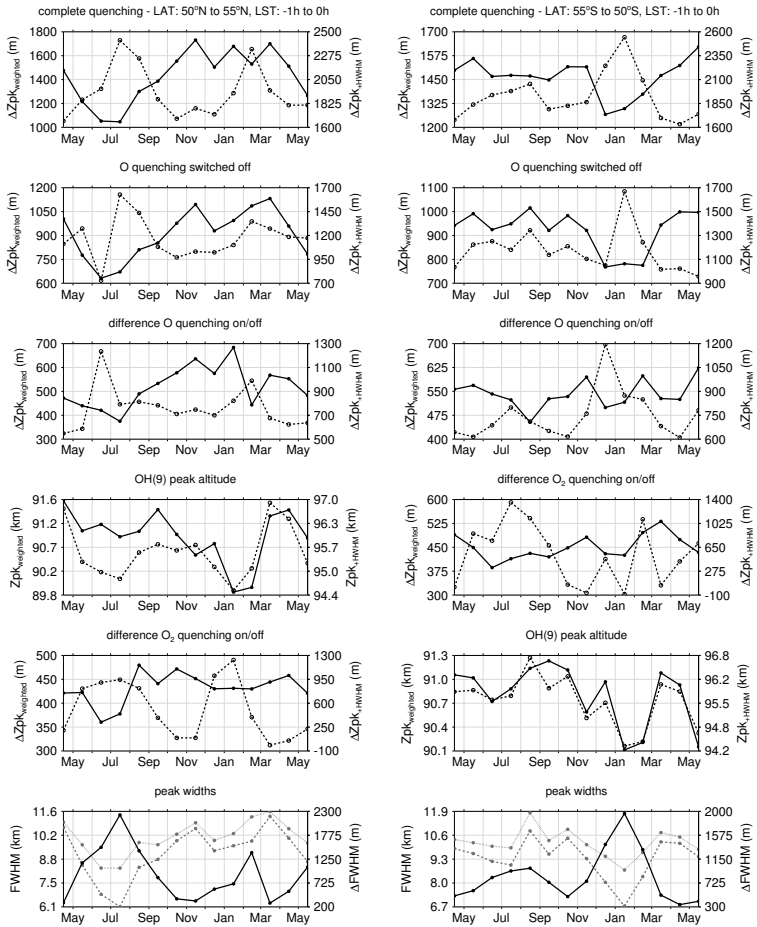

Fig. 13. Seasonal variability of OH peak shifts for different model runs in the latitudinal range from 50° N to 55° N (left panels) and from 50° S to 55° S right panels. Same conventions apply as for the equatorial example in Fig. 11.

ACPD
14, 1239–1285, 2014

CC BY

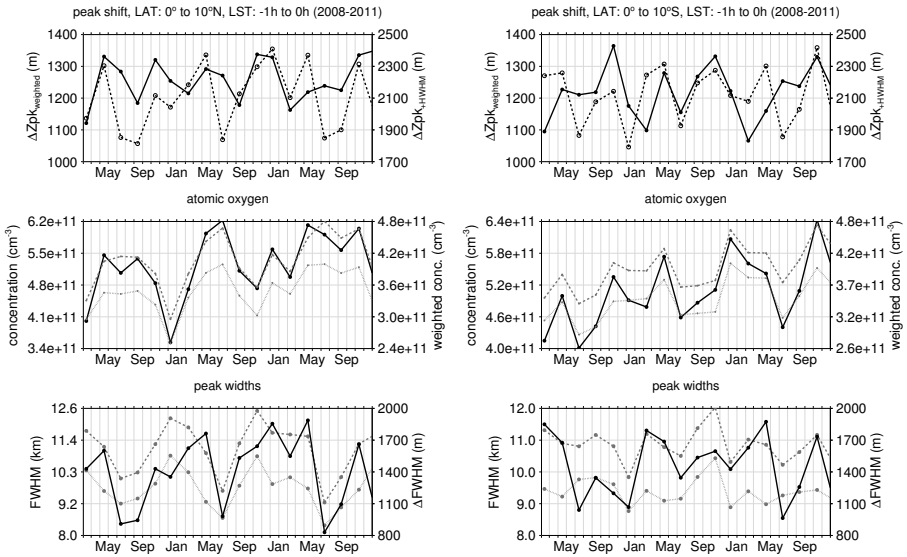

Fig. 14. Seasonal variability of OH peak shifts, atomic oxygen and OH* layer peak width based on SABER observations. Right panels: latitude range from 10° S to 0°. Left panels: latitude range from 0° to 10° N. Same denotations apply for all three parameters as those used in Fig. 9.

ACPD
14, 1239–1285, 2014

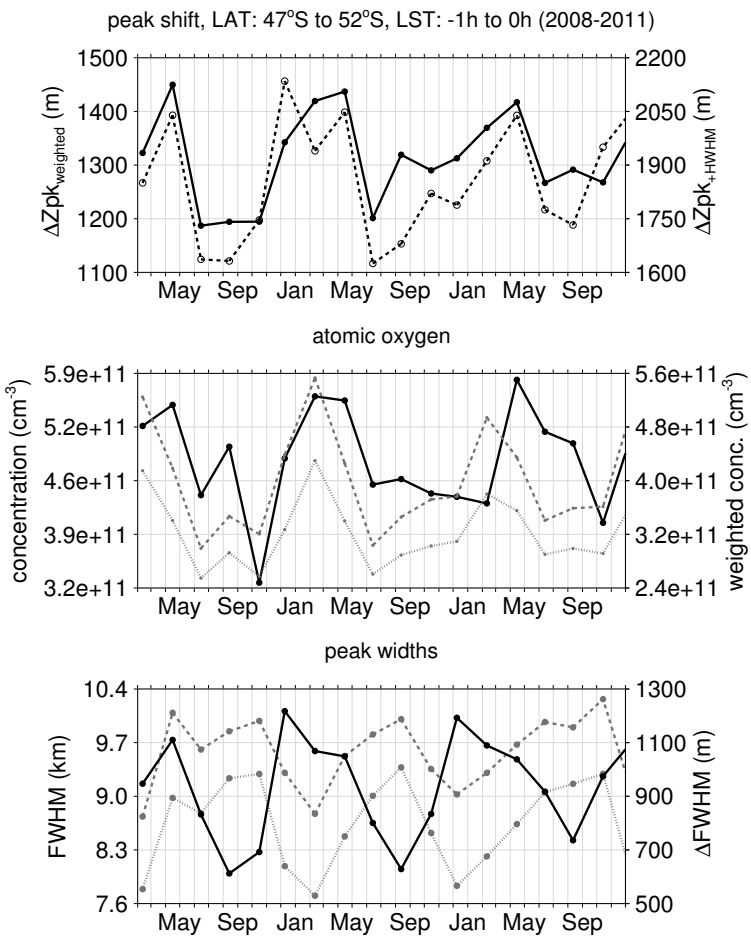

Fig. 15. Similar to Fig. 14 but for the latitude range from 47° S to 52° S.

ACPD
14, 1239–1285, 2014